Effect of dehydration reactions on earthquake nucleation: Stable sliding, slow transients and unstable slip

Nicolas Brantut, Jean Sulem, Alexandre Schubnel

To cite this version:

Nicolas Brantut, Jean Sulem, Alexandre Schubnel. Effect of dehydration reactions on earthquake nucleation: Stable sliding, slow transients and unstable slip. Journal of Geophysical Research, 2011, 116, pp.B05304. 10.1029/2010JB007876 . hal-00688220

JOURNAL OF GEOPHYSICAL RESEARCH, VOL. 116, B05304, doi:10.1029/2010JB007876, 2011

Effect of dehydration reactions on earthquake nucleation: Stable sliding, slow transients, and unstable slip

N. Brantut,[1] J. Sulem,[2] and A. Schubnel[1]

Received 22 July 2010; revised 1 December 2010; accepted 22 February 2011; published 18 May 2011.

[1] We study the influence of metamorphic dehydration reactions on the stability of slip in a one-dimensional, spring-slider model. The equations that govern the evolution of the velocity of sliding block and of pore pressure and temperature inside the slip zone are deduced from the mass and energy balance of the multiphases saturated medium and from the kinetics of the dehydration reaction. Such reactions induce two competing effects: a direct increase in pore pressure because they release fluid and a limit in temperature increase because part of the frictional heat is absorbed in the endothermic reactions. The effect of the chemical reaction on the stability of stationary slip is studied. Dehydration reactions increase the critical stiffness at which the system becomes unstable. Depending on the sign of the perturbations, it is shown that dehydration reactions can either (1) trigger a catastrophic increase of pore pressure at quasi-constant temperature leading to vanishing effective stress or (2) trigger an arrest of the fault. Numerical simulations demonstrate the crucial role of initial pore pressure and temperature in the slip zone prior to the onset of the chemical reaction on the subsequent evolution of the system. For highly pressurized fault zones, in which the creep motion of the fault is stable in absence of dehydration reactions, the onset of the reaction can trigger transient slip events induced by chemical pressurization. The magnitude of such events appears to be proportional to the reaction progress. We conclude that metamorphic dehydration reactions strongly modify the nucleation of unstable slip and are a possible origin for slow slip events in subduction zones.

Citation: Brantut, N., J. Sulem, and A. Schubnel (2011), Effect of dehydration reactions on earthquake nucleation: Stable sliding, slow transients, and unstable slip, *J. Geophys. Res.*, *116*, B05304, doi:10.1029/2010JB007876.

1. Introduction

[2] Earthquake nucleation and slip instability occur because the frictional resistance to slip on the fault walls decreases with slip (and/or slip rate), causing an acceleration of sliding. The shear resistance τ is classically expressed as proportional to the Terzaghi effective stress: $\tau = f(\sigma_n - p)$, where σ_n is the normal stress acting on the fault, p is the pore pressure and f is the friction coefficient. A decreasing evolution of τ with increasing displacement can be induced by a change of either of these three factors. In the last 30 years there have been extensive studies to understand the dependency of friction coefficient with slip, slip rate, surface state and temperature [*Dietrich*, 1978, 1979; *Marone et al.*, 1990; *Chester*, 1994; *Marone*, 1998], leading to the formulation of the rate-and-state friction laws [*Ruina*, 1983]. The normal stress can also change during slip due to wavy fault surfaces and geometrical incompatibilies. Finally, the pore pressure can also evolve because of (1) dilatancy or compaction [*Marone et al.*, 1990], (2) fluid diffusion outside the shear zone, (3) shear heating and induced pore fluid pressurization, and (4) thermal decomposition reactions of unstable minerals inside the shear zone. The three first effects have already been widely studied, either separately [*Garagash and Rudnicki*, 2003a, 2003b; *Suzuki and Yamashita*, 2006, 2007] or combined with rate-and-state friction laws [*Segall and Rice*, 2006]. In particular, *Segall and Rice* [2006] have shown that shear heating and induced pore fluid pressurization becomes significant only when the slip rate is already high (~ cm/s), and thus the onset of earthquake nucleation cannot be attributed solely to this effect. The role of dehydration reactions has not been yet considered for the nucleation of unstable slip.

[3] Recent data on fault rocks mineralogy [e.g., *Sulem et al.*, 2004; *Solum et al.*, 2006; *Hirono et al.*, 2008] have revealed the presence of a significant amount of clays and hydrous phyllosilicates along major subsurface fault zones. These types of minerals are thermally unstable and can release adsorbed and/or structural water while turning into a denser reaction product. At relatively low pressure (below gigapascal), such reactions induce a total volume increase; that is, the total molar volume of the reaction products (including

---

[1] Laboratoire de Géologie, CNRS, UMR 8538, École Normale Supérieure, Paris, France.

[2] CERMES, UR Navier, CNRS, UMR 8205, École des Ponts ParisTech, Université Paris-Est, Marne-la Vallée, France.

0148-0227/11/2010JB007876

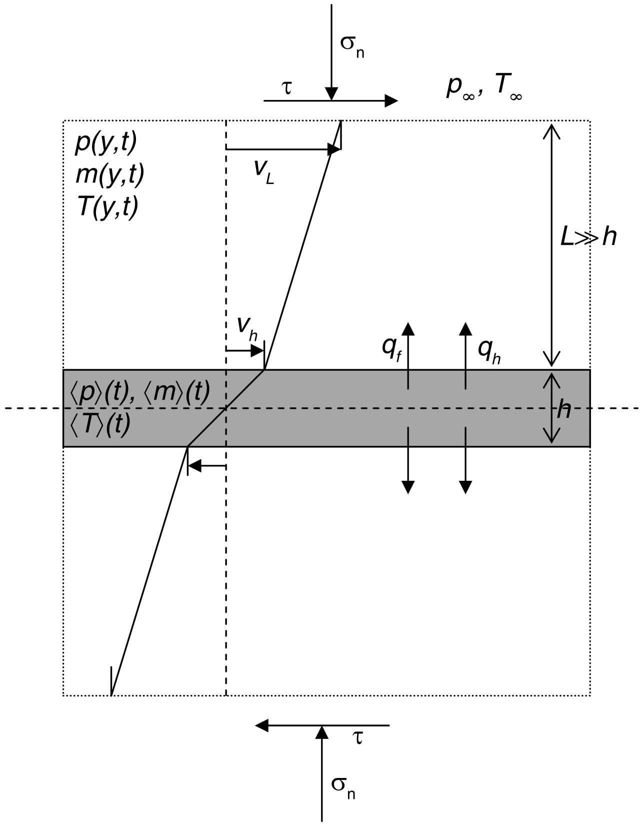

Figure 1. Model of a deforming shear band with heat and fluid fluxes.

water) is higher than the molar volume of the reactant. Consequently, dehydration or dehydroxylation reactions can increase the pore pressure. The subsequent reduction of the effective mean stress can induce a macroscopic rupture, which has been observed experimentally [*Raleigh and Paterson*, 1965; *Heard and Rubey*, 1966; *Murrell and Ismail*, 1976; *Olgaard et al.*, 1995; *Milsch and Scholz*, 2005]. In addition, the endothermic character of such chemical reactions play also a major role in the energy balance of the system, as a part of the frictional heat is consumed by the reaction. Their effect on long-runout landslides has been recently studied by *Goren et al.* [2010]. This process has already been shown to influence faults mechanical behavior during seismic slip [*Sulem and Famin*, 2009; *Brantut et al.*, 2010; *Veveakis et al.*, 2010]. In this work we investigate their effect on the stability of stationary fault motion.

[4] The aim of this study is to explore coupled processes of shear heating, chemical reactions and pore fluid pressurization. Thus, we do not account for other processes mentioned above, such as changes in friction coefficient and total normal stress. The questions addressed are (1) whether mineral decomposition reactions can influence the creep motion of a fault and (2) whether they can destabilize the fault motion into accelerating slip. Following the approach of *Garagash and Rudnicki* [2003a], we first derive the governing equations for a one-dimensional model of a fault zone that undergoes a remote, slow loading. We then discuss a set of representative parameters and their corresponding geological setting. A linear perturbation analysis is performed to investigate the stability regimes. Finally, we present some numerical examples using an Arrhenius law for the reaction kinetic. We show that dehydration reactions can either accelerate or decelerate the fault motion, depending on initial state and parameter values. Interestingly, dehydration reactions are shown to destabilize a fault motion that would otherwise be stable, leading to transient accelerated slip events.

2. Model Description

[5] Figure 1 shows the geometry of the problem and the far field loading conditions. A crustal block of thickness $2L$ contains a shear band of thickness h with $h \ll L$. Considering that the length scales in the direction parallel to the fault over which the thermoporomechanical fields vary are much larger than in the direction normal to it, we analyze here a 1D problem. The pore pressure $p(t, y)$, the temperature $T(t, y)$, and the velocity $v(t, y)$ are assumed to be functions of time t only and of the position y in the direction normal to the band.

2.1. Stress Equilibrium

[6] Because we neglect inertial effects, the shear stress τ and the total normal stress σ_n are uniform throughout the layer. The material inside the shear band ($|y| < h/2$) undergoes inelastic loading whereas the material inside the crustal block ($h/2 < |y| < h/2 + L$) behaves elastically. Thus the shear stress in the crustal block is given by the elastic relation

$$\tau = G\left(\frac{D_L - D_h}{L}\right), \tag{1}$$

where G is the shear modulus, D_L is the slip displacement at $y = h/2 + L$, and D_h is the slip displacement at $y = h/2$.

[7] Inside the shear band, it is assumed that the frictional resistance is proportional to the mean effective stress inside the band:

$$\tau = f(\sigma_n - \langle p \rangle), \tag{2}$$

where f is the friction coefficient of the material and $\langle p \rangle$ is the mean pore pressure inside the shear band. Because equilibrium requires uniform shear stress, expressions (1) and (2) must be equal:

$$G\left(\frac{D_L - D_h}{L}\right) = f(\sigma_n - \langle p \rangle). \tag{3}$$

The slip velocity v_h at the shear band boundary is thus given by

$$v_h = v_L + f\frac{L}{G}\frac{d\langle p \rangle}{dt}, \tag{4}$$

where v_L is boundary condition for the slip rate at $y = h/2 + L$.

2.2. Mass Balance Equation

[8] Conservation of fluid mass is expressed by

$$\frac{\partial m_f}{\partial t} = \frac{\partial m_d}{\partial t} - \frac{\partial q_f}{\partial y}, \tag{5}$$

where m_f is the total fluid mass per unit volume of porous medium (in the reference state), m_d is the mass per unit volume of the fluid released in the system by mineral decomposition, and q_f is the fluid flux. The total fluid mass per unit volume of porous medium is written as $m_f = \rho_f n$, where n is the pore volume fraction (Lagrangian porosity) and ρ_f is the density of the saturating fluid. The left hand side of equation (5) is obtained by differentiating this product:

$$\frac{\partial m_f}{\partial t} = n\frac{\partial \rho_f}{\partial t} + \rho_f \frac{\partial n}{\partial t}. \tag{6}$$

The derivatives of the right-hand side of equation (6) are given by

$$\frac{\partial \rho_f}{\partial t} = \rho_f \beta_f \frac{\partial p}{\partial t} - \rho_f \lambda_f \frac{\partial T}{\partial t}, \tag{7}$$

$$\frac{\partial n}{\partial t} = n\beta_n \frac{\partial p}{\partial t} - n\lambda_n \frac{\partial T}{\partial t} + \frac{\partial n_d}{\partial t}, \tag{8}$$

where $\beta_f = (1/\rho_f)(\partial \rho_f/\partial p)_T$ is the pore fluid compressibility, $\lambda_f = (-1/\rho_f)(\partial \rho_f/\partial T)_p$ is the pore fluid thermal expansion coefficient, $\beta_n = (1/n)(\partial n/\partial p)_T$ is the pore volume compressibility, and $\lambda_n = (1/n)(\partial n/\partial T)_p$ is the pore volume thermal expansion coefficient. The latter parameter is equal to the thermal expansion coefficient of the solid fraction for thermoporoelastic materials. In equation (8), $\partial n_d/\partial t$ is the rate of inelastic porosity change. This term includes the effect of coseismic dilatancy induced by fault surface irregularities and the solid volume change of the mineral decomposition reaction.

[9] Using equations (7) and (8), the left-hand side of equation (5) is thus evaluated as [see also *Rice*, 2006; *Sulem et al.*, 2007]

$$\frac{\partial m_f}{\partial t} = n\rho_f(\beta_n + \beta_f)\frac{\partial p}{\partial t} - n\rho_f(\lambda_f - \lambda_n)\frac{\partial T}{\partial t} + \rho_f \frac{\partial n_d}{\partial t}. \tag{9}$$

Using this relation, equation (5) can be rewritten as

$$-\frac{\partial q_f}{\partial y} = n\rho_f(\beta_n + \beta_f)\frac{\partial p}{\partial t} - n\rho_f(\lambda_f - \lambda_n)\frac{\partial T}{\partial t} + \rho_f \frac{\partial n_d}{\partial t} - \frac{\partial m_d}{\partial t}. \tag{10}$$

The flux term in equation (10) is evaluated assuming Darcy's law for fluid flow with viscosity η_f through a material of permeability k_f:

$$q_f = -\frac{\rho_f}{\eta_f} k_f \frac{\partial p}{\partial y}. \tag{11}$$

Substituting this relation into (10) yields the equation that governs the pore fluid production and diffusion:

$$\frac{\partial p}{\partial t} = \frac{1}{\rho_f \beta^*}\frac{\partial}{\partial y}\left(\frac{\rho_f}{\eta_f} k_f \frac{\partial p}{\partial y}\right) + \Lambda \frac{\partial T}{\partial t} + \frac{1}{\rho_f \beta^*}\frac{\partial m_d}{\partial t} - \frac{1}{\beta^*}\frac{\partial n_d}{\partial t}, \tag{12}$$

where

$$\Lambda = \frac{\lambda_f - \lambda_n}{\beta_f + \beta_n} \tag{13}$$

is the thermoelastic pressurization coefficient under undrained conditions [*Rice*, 2006] and $\beta^* = n(\beta_n + \beta_f)$ is the storage capacity of the rock. This coefficient is pressure and temperature dependent because the compressibility and the thermal expansion coefficients of the fluid vary with pressure and temperature, and also because the compressibility of the pore space of the rock can change with effective stress [*Ghabezloo and Sulem*, 2009].

[10] In the following, we shall neglect the effect of dilatancy induced by fault surface irregularities, and only consider the effect of the decomposition of the solid phase on porosity changes. For example, in a fault zone through a serpentinite rock, dehydration of serpentine induces a water release. If the serpentine mineral is lizardite we obtain

$$\begin{aligned} 5\ \mathrm{Mg_3Si_2O_5(OH)_4} \rightarrow\ & \mathrm{Mg_3Si_4O_{10}(OH)_2} \\ & +6\ \mathrm{Mg_2SiO_4} + 9\ \mathrm{H_2O}. \end{aligned} \tag{14}$$

The rate of water release is evaluated using the kinetic of the chemical reaction. Assuming a first-order reaction mechanism, the mass m_d of released water per unit volume is expressed as

$$\frac{\partial m_d}{\partial t} = \kappa(T)(m_0 - m_d), \tag{15}$$

where $\kappa(T)$ is the kinetic parameter and m_0 is the total mass of water that can be released per unit of rock volume. The value of m_0 is calculated considering the stoechiometry of the reaction and the mass fraction of dehydrating mineral in the bulk rock. For instance, if we consider the dehydration of pure lizardite (equation (14)), we get $m_0 = (9/5) \times \rho_{\mathrm{lizardite}} M_{\mathrm{H_2O}}/M_{\mathrm{lizardite}}$, where $\rho_{\mathrm{lizardite}}$ is the density of lizardite, $M_{\mathrm{lizardite}}$ is the molar mass of lizardite and $M_{\mathrm{H_2O}}$ is the molar mass of water. The dependency of $\kappa(T)$ on temperature can be expressed by an Arrhenius law in the form

$$\kappa(T) = A\exp\left(-\frac{E_a}{RT}\right), \tag{16}$$

where A is a constant (preexponential term of the Arrhenius law), E_a is the activation energy of the reaction and R is the gas constant (8.314 J $°\mathrm{K}^{-1}$ mol^{-1}). Thus the mass m_d of released water per unit volume is expressed as

$$\frac{\partial m_d}{\partial t} = (m_0 - m_d)A\exp\left(-\frac{E_a}{RT}\right). \tag{17}$$

The rate of inelastic porosity change due to the reaction is expressed as

$$\rho_f \frac{\partial n_d}{\partial t} = \xi \frac{\partial m_d}{\partial t}, \tag{18}$$

where ξ corresponds to the ratio of the volume of voids over the volume of fluid formed by the reaction. The pore volume created during the reaction can be plastically compacted at high effective stress, thus the evolution of n_d can be affected by compaction. Considering only the volume change of the reaction gives an upper bound of the porosity change. A reduced ξ value could be used to simulate additional compaction.

2.3. Energy Balance

[11] Let E_F be the rate of frictional heat produced during slip and E_C the rate of heat used in the endothermic thermal decomposition. The equation of energy conservation is expressed as

$$\rho C \frac{\partial T}{\partial t} = E_F + E_C - \frac{\partial q_h}{\partial y}, \tag{19}$$

where ρC is the specific heat per unit volume of the fault material in its reference state and q_h is the heat flux. The fraction of plastic work converted into heat is represented by the Taylor-Quinney coefficient. For metals this coefficient takes values between 0.2 and 0.9 and the remainder contributes to the stored energy of cold work due to the creation of crystal defects [*Rosakis et al.*, 2000]. In rocks, energy can be taken up by the creation of new mineral surfaces when grain size is reduced during deformation. During rapid earthquake slip (slip rate of the order of 1 m s^{-1}), dramatic changes in grain size are expected [*Chester et al.*, 2005; *Brantut et al.*, 2008] and the surface energy may correspond to a significant energy sink. Here we neglect this energy sink by considering that the fault rock within the shear zone has a steady state microstructure. Such an assumption is appropriate since we are only dealing with long-term, slow slip and the early stages of earthquake nucleation. All the plastic work is thus converted into heat, which leads to $E_F = \tau(\partial v/\partial y)$ inside the band ($|y| \leq h/2$) and $E_F = 0$ in the elastic deforming block.

[12] As the reaction progresses, energy is absorbed due to the enthalpy change of the system. The rate of heat used in the chemical reaction can be expressed from the enthalpy change of the reaction and the rate of reacted fraction:

$$E_C = \Delta_r H_T \frac{\partial m_d}{\partial t}, \tag{20}$$

where $\Delta_r H_T$ is the enthalpy change per unit mass of the dehydrating mineral. Equation (19) is rewritten as follows:

$$-\frac{\partial q_h}{\partial y} = \rho C \frac{\partial T}{\partial t} - E_F + \Delta_r H_T \frac{\partial m_d}{\partial t}. \tag{21}$$

The heat flux is related to the temperature gradient by Fourier's law:

$$q_h = -k_T \frac{\partial T}{\partial y}, \tag{22}$$

where k_T is the thermal conductivity of the saturated material. In equation (19) it is assumed that all heat flux is due to heat conduction neglecting heat convection by the moving hot fluid. This assumption is justified by the low pore volume fraction and the low permeability of fault gouges [*Lee and Delaney*, 1987]. However, this assumption should be relaxed in case of a high permeability in the wall rocks of the fault. Substituting (22) into (19) gives the temperature evolution equation

$$\rho C \frac{\partial T}{\partial t} = \tau \frac{\partial v}{\partial y} + \Delta_r H_T \frac{\partial m_d}{\partial t} + \frac{\partial}{\partial y}\left(k_T \frac{\partial T}{\partial y}\right). \tag{23}$$

2.4. Averaged Fields Inside the Shear Band

[13] Considering the extreme thinness of the shear band as observed in faults zones (from few millimeters to few centimeters [cf. *Rice*, 2006, and references therein]), it is relevant to consider mean values for the pore pressure and temperature fields inside the slip zone. Let $\langle p \rangle$ and $\langle T \rangle$ be the mean pore pressure and temperature inside the shear band. The mean pore pressure is calculated as

$$\langle p \rangle(t) = \frac{1}{h}\int_{-h/2}^{h/2} p(y,t)\,dy, \tag{24}$$

and similar formulas hold for the spatial average of any quantity such as temperature and mass of fluid. Since we assume that the shear band thickness h does not evolve in time, the time derivative of mean pore pressure is

$$\frac{d\langle p \rangle(t)}{dt} = \frac{1}{h}\int_{-h/2}^{h/2} \frac{\partial p(y,t)}{\partial t}\,dy. \tag{25}$$

Equations (10) and (21) can thus be averaged over the shear band thickness to obtain the pore pressure and temperature gradients at the shear band boundaries:

$$\left.\frac{\partial p}{\partial y}\right|_{h/2} = \frac{h}{2}\frac{\eta_f}{\rho_f k_f}\left[\rho_f \beta^* \left(\frac{d\langle p \rangle}{dt} - \Lambda \frac{d\langle T \rangle}{dt}\right) + (\xi - 1)\frac{d\langle m_d \rangle}{dt}\right], \tag{26}$$

$$\left.\frac{\partial T}{\partial y}\right|_{h/2} = \frac{1}{k_T}\left[\frac{h}{2}\rho C \frac{d\langle T \rangle}{dt} - \tau v_h - \frac{h}{2}\Delta_r H_T \frac{d\langle m_d \rangle}{dt}\right]. \tag{27}$$

At this point, a useful simplification can be made by considering the averaged quantities $\langle p \rangle$ and $\langle T \rangle$ as boundary conditions at $y = h/2$. This assumption holds when the shear band thickness is very small compared to heat and fluid diffusion lengths, which is the case at the long time scales investigated here. In order to simplify the notations, in the following we reset the origin of y axis at $h/2$, applying

$$y \leftarrow y - h/2.$$

The average rate of released fluid inside the shear band can be expressed from the kinetic law (17) as a function of the mean temperature $\langle T \rangle(t)$,

$$\frac{d\langle m_d \rangle}{dt} = (\langle m_0 \rangle - \langle m_d \rangle) A \exp\left(-\frac{E_a}{R\langle T \rangle}\right). \tag{28}$$

2.5. Dimensionless Formulation

[14] The number of parameters introduced in the governing equations can be reduced by choosing appropriate dimensional quantities to scale the variables. We define

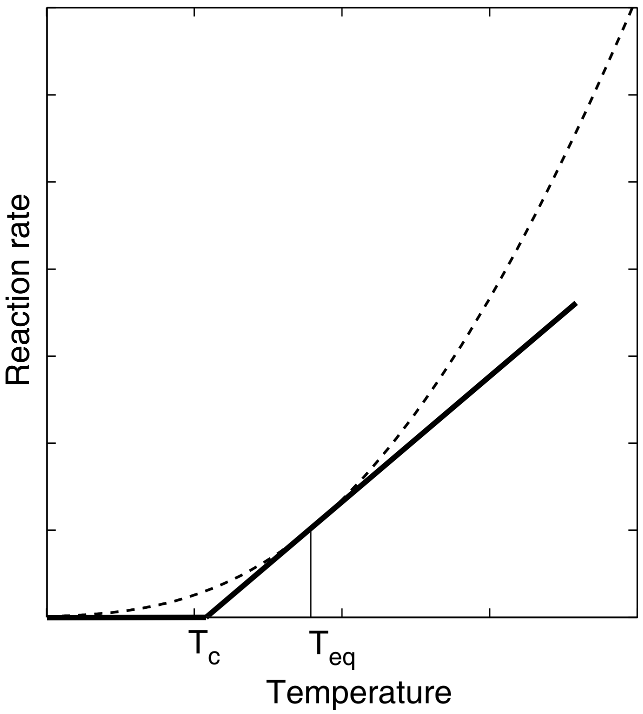

Figure 2. Linearization of the Arrhenius law (dashed line) around T_{eq}. The threshold temperature T_{c} is the intersect of the slope with the T axis.

characteristic time t^*, length y^*, pore pressure p^*, temperature T^*, fluid mass m^*, and slip velocity v^* as follows:

$$t^* = \rho C L^2/k_{\mathrm{T}}, \quad y^* = L, \quad p^* = \sigma_{\mathrm{n}}, \quad T^* = \frac{\sigma_{\mathrm{n}}}{\Lambda} \\ v^* = v_{\mathrm{L}}, \quad \text{and } m^* = m_0. \tag{29}$$

The dimensionless time $\tilde{t}$, length $\tilde{y}$, pore pressure π, temperature θ, velocity u, and mass of released fluid μ are

$$\tilde{t} = t/t^*, \quad \tilde{y} = y/L, \quad \pi = p/p^*, \quad \theta = T/T^*, \\ u = v_{\mathrm{h}}/v^*, \quad \text{and } \mu = m_{\mathrm{d}}/m_0. \tag{30}$$

Equations (4), (12), (23), (17), and boundary conditions (26) and (27) can then be rewritten as

$$u = 1 + \mathcal{A}\partial_t\langle\pi\rangle, \tag{31}$$

$$\partial_t\pi = \epsilon\partial_{yy}\pi + \partial_t\theta + \mathcal{P}\partial_t\mu, \tag{32}$$

$$\partial_t\theta = \partial_{yy}\theta + \mathcal{T}\partial_t\mu, \tag{33}$$

$$\partial_t\mu = (1-\mu)m_0 A t^* e^{-\frac{E_a}{RT^*}\theta}, \tag{34}$$

$$\left.\frac{\partial\pi}{\partial y}\right|_{y=0} = \frac{\delta}{\epsilon}\left(\partial_t\langle\pi\rangle - \partial_t\langle\theta\rangle - \mathcal{P}\partial_t\mu\right), \tag{35}$$

$$\left.\frac{\partial\theta}{\partial y}\right|_{y=0} = -\mathcal{B}(1-\langle\pi\rangle)u + \delta\left(\partial_t\langle\theta\rangle - \mathcal{T}\partial_t\mu\right), \tag{36}$$

where ∂_t denotes the derivative with respect to the dimensionless time $\tilde{t}$, and ∂_{yy} denotes the second derivative with respect to the dimensionless length $\tilde{y}$. In the following and throughout the rest of the text we note $t \equiv \tilde{t}$ and $y \equiv \tilde{y}$. The remote boundary conditions are $\pi(y = 1) = \pi_\infty = p_\infty/p^*$ and $\theta(y = 1) = \theta_\infty = T_\infty/T^*$.

[15] In the normalized equations, six dimensionless parameters are introduced:

$$\mathcal{P} = m_0\frac{1-\xi}{\rho_{\mathrm{f}}\beta^*}\frac{1}{\sigma_{\mathrm{n}}}, \quad \mathcal{T} = m_0\frac{\Delta_{\mathrm{r}}H_T}{\rho C}\frac{1}{\sigma_{\mathrm{n}}/\Lambda}, \quad \mathcal{A} = f\frac{\sigma_{\mathrm{n}}}{G}\frac{\alpha_{\mathrm{th}}}{v_L L}, \\ \mathcal{B} = f\frac{v_L L}{\alpha_{\mathrm{th}}}\frac{\Lambda}{\rho C}, \quad \epsilon = \frac{\alpha_{\mathrm{hy}}}{\alpha_{\mathrm{th}}}, \quad \delta = \frac{h}{2L}, \tag{37}$$

where $\alpha_{\mathrm{th}} = k_{\mathrm{T}}/(\rho C)$ is the heat diffusivity; $\alpha_{\mathrm{hy}} = k_{\mathrm{f}}/(\eta_{\mathrm{f}}\beta^*)$ is the fluid diffusivity; and (1) $\mathcal{P}$ relates the rate of reacted fraction with the pore pressure change and combines the effect of porosity changes due to the reaction and to possible compaction mechanisms, (2) $\mathcal{T}$ relates the rate of reacted fraction with the temperature change and is negative for endothermal reactions, (3) $\mathcal{A}$ relates the pore pressure change with the velocity change of the sliding block, (4) $\mathcal{B}$ relates the dimensionless frictional work with the temperature change (shear heating effect), (5) ϵ compares the efficiency of fluid diffusion to heat diffusion, and (6) δ is the normalized thickness of the shear zone.

[16] The case of no reaction corresponds to $\mathcal{P} = \mathcal{T} = 0$. The asymptotic case of $\mathcal{A} \rightarrow 0$ corresponds to an infinitely stiff loading medium, which ensures a stable slip on the fault [e.g., *Scholz*, 2002]. The case of $\epsilon = 0$ corresponds to the undrained limit. A truly adiabatic limit cannot be realistically simulated by our set of equations because we chose the heat diffusion time as the characteristic time scale. However, setting a large ϵ can simulate a rock mass that is well thermally insulated.

2.6. Reaction Kinetic

[17] The Arrhenius law used in the constitutive equations is highly nonlinear with temperature. In order to get simple insights on the stability of the system this law can be linearized around the temperature of equilibrium of the reaction T_{eq}. Theoretical studies [*Sulem and Famin*, 2009; *Brantut et al.*, 2010] have shown that temperature is efficiently buffered around the equilibrium temperature of the reaction during a slip event. Thus, temperature is not expected to increase far from T_{eq} when the reaction occurs. From the linearization we can define a threshold temperature T_{c}, below which no reaction occurs, and above which the reaction starts with a kinetic linearly dependent on temperature. In addition, we assume that the reaction rate is not limited by the amount of dehydrating mineral, i.e., $\mu \ll 1$. These assumptions correspond to the beginning of the reaction, when there is still a large amount of minerals to dehydrate, and when the temperature has just reached

Table 1. Typical Parameter Values for a Fault at 7 km Depth

Physical Parameter	Symbol	Typical Value	Unit
Forcing velocity	v_L	10^{-9}	$\mathrm{m\ s^{-1}}$
Size of the crustal block	L	10^4	m
Elastic stiffness of the crustal block	G	$30\ 10^9$	Pa
Friction coefficient	f	0.5	
Fluid density	ρ_f	10^3	$\mathrm{kg\ m^{-3}}$
Storage capacity	β^*	10^{-9}	$\mathrm{Pa^{-1}}$
Fluid diffusivity	α_hy	10^{-6} to 10^{-3}	$\mathrm{m^2\ s^{-1}}$
Thermal pressurization factor	Λ	0.510^6	$\mathrm{Pa\ C^{\circ -1}}$
Void creation vs fluid release ratio	ξ	0.8	
Specific heat capacity	ρC	$2.7\ 10^6$	$\mathrm{Pa\ C^{\circ -1}}$
Heat diffusivity	α_th	10^{-6}	$\mathrm{m^2\ s^{-1}}$
Enthalpy of the reaction	$\Delta_\mathrm{r} H_T^0$	−500	$\mathrm{kJ\ kg^{-1}}$
Normal stress	σ_n	$200\ 10^6$	Pa
Mass of released fluid	m_0	10^2	$\mathrm{kg\ m^{-3}}$
Width of the slipping zone	h	10^{-1} to 10^{-3}	m

the equilibrium temperature. The linearization process is represented graphically on Figure 2.

[18] For convenience, in the following and throughout the text we shift the temperature values, applying $\theta \leftarrow \theta - \theta_\mathrm{c}$, where $\theta_\mathrm{c} = T_\mathrm{c}/T^*$. The onset of the reaction thus corresponds to $\theta = 0$. We can express the reaction rate as

$$\partial_t \mu \sim \begin{cases} 0 & \text{if } \theta \leq 0 \\ c^* \theta & \text{if } \theta > 0 \end{cases}. \tag{38}$$

3. Representative Parameters

[19] The set of parameters introduced in the constitutive equations needs to be constrained by laboratory and field data. On the basis of field and experimental data from the literature [*Wibberley*, 2002; *Wibberley and Shimamoto*, 2003; *Noda and Shimamoto*, 2005; *Mizoguchi*, 2005] and representative parameters used by *Garagash and Rudnicki* [2003a], *Rice* [2006], *Segall and Rice* [2006], and *Sulem and Famin* [2009] we consider the values reported on Table 1. The type of fault considered in the following is situated at the midseismogenic depth of 7 km, corresponding to a normal stress of 200 MPa and an initial pore pressure of 70 MPa. An other deeper setting will be introduced and investigated in section 5. The initial and remote temperature is 210 °C. The friction coefficient is of the order of 0.5, considering that clay minerals are present within the fault rock. The typical value of the thermal pressurization parameter Λ is taken equal to 0.5 [*Rice*, 2006; *Rempel and Rice*, 2006; *Sulem and Famin*, 2009; *Brantut et al.*, 2010]. The heat diffusivity does not strongly depend on the rock type, and is set to 10^{-6} m^2 s^{-1}. Water diffusivity may vary from 10^{-6} m^2 s^{-1} to 10^{-3} m^2 s^{-1} depending on the rock type and its porosity and pore connectivity. Such values correspond to permeabilities ranging from 10^{-20} m^2 to 10^{-17} m^2.

[20] The shear zone thickness may range from a few centimeters down to a few millimeters in a case of an extremely localized shear zone. At seismic slip rates, it can be even thinner but we restrain our study to a slowly deforming region.

[21] The loading distance L is not easily constrained because the geometry of the fault is oversimplified. However, *Segall and Rice* [2006] suggest an order of 10 km. The elastic shear modulus of the surrounding rock mass is set at 30 GPa. The remote loading velocity can be chosen as an average for plate motion velocity, i.e., few centimeters per year. This yields $v_\mathrm{L} \sim 10^{-9}$ m s^{-1}.

[22] The parameters linked to the chemistry of the rock depend of the particular reaction considered and the amount of dehydrating minerals. Investigating a general behavior, we choose typical values. Concerning the enthalpy of dehydration reactions, data can be found in the work of *Hamada et al.* [2009, and references therein] and is of the order of $\Delta_\mathrm{r} H_T \sim -0.5$ kJ kg^{-1}.

[23] The mass of released water per unit of rock volume is calculated from the stoechiometry of the reaction and the amount of dehydrating mineral within the total rock mass. Typically, a pure serpentinite can release up to 15 wt% of water, which yields $m_0 = 400$ kg m^{-3}. A fault rock containing 20 wt% of kaolinite can release up to 2.4 wt% of water, i.e., $m_0 = 65$ kg m^{-3} [*Brantut et al.*, 2008]. These two examples can be seen as upper bounds for m_0, so we use an average value of $m_0 = 100$ kg m^{-3}.

[24] The ratio of inelastic porosity increase over fluid volume production ξ is less than one; that is, the total volume change is positive. It is estimated from the molar volumes of the reaction products compared to that of the starting mineral. For example, the reaction from lizardite to forsterite, talc and water (equation (14)) creates around 26 % porosity, and up to 38 % of pore fluid volume at 70 MPa pore pressure and confining pressure, and 450°C [*Robie et al.*, 1979]. This yields $\xi \approx 0.7$. For kaolinite dehydroxylation, there are no data on the molar volume of the reaction product (metakaolinite). However, similar estimates performed on various dehydration reactions of antigorite, chrysotile, talc and various hydrous phyllosiilicates yield values of ξ ranging from 0.7 to 0.9. Thus we use an average of $\xi = 0.8$.

[25] The least constrained parameter is certainly the kinetic parameter c^*. It corresponds to the slope of the kinetic rate as a function of temperature. Using the kinetic parameters reported on Table 2, we perform a Taylor expansion of the Arrhenius law around $T_\mathrm{eq} = 500$°C for kaolinite decomposition reaction. Using parameter values from *Saikia et al.* [2002], we find an expansion in the form of $A \exp(-E_\mathrm{a}/RT) \sim 4.8\ 10^{-5} + 1.9\ 10^{-6}\ (T - T_\mathrm{eq})$. It yields $T_\mathrm{c} \approx 475$°C. Similarly, for lizardite decomposition around $T_\mathrm{eq} = 500$°C we use kinetic data from *Llana-Fúnez et al.* [2007] to get an expansion of the form $4.7 \times 10^{-5} + 3.2 \times 10^{-6}\ (T - T_\mathrm{eq})$. The temperature of initiation is then $T_\mathrm{c} \approx 485$°C. The slope values need to be normalized by the reference time scale L^2/α_th and temperature scale $\sigma_\mathrm{n}/\Lambda$ to obtain the nondimensional c^* value. Using values from kaolinite decompostion we obtain $c^* \approx 7.6 \times 10^{10}$ and for lizardite $c^* \approx 12.7 \times 10^{10}$. These very large values imply that the dehydration reaction proceeds rapidly compared to diffusion and frictional heating processes. It will thus be the dominant phenomenon as soon as it starts.

[26] The threshold temperature T_c depends strongly on the mineral of interest. We consider here a fault containing hydrous phyllosilicates. Kaolinite has been found in Chelung-Pu fault gouge (Taiwan) and along an exhumated section of the Median Tectonic Line (Japan) [*Hirono et al.*, 2008; *Brantut et al.*, 2008]. Its dehydration temperature is around 500°, i.e., 300°C above the ambient temperature.

Table 2. Examples of Kinetic Parameters Used in the Calculations[a]

Mineral	A (s^{-1})	E_a (kJ mol^{-1})	T_{eq} (°C)	T_c (°C)	c*
Kaolinite	9.57 10^{8}	196.8	500	475	7.6 10^{10}
Lizardite	3.14 10^{18}	328	500	485	12.2 10^{11}

[a]Kaolinite dehydroxylation data are from *Saikia et al.* [2002], and lizardite dehydration data are from *Llana-Fúnez et al.* [2007].

Serpentine minerals such as lizardite has been found in subsurface faults such as San Andreas [*Solum et al.*, 2006] and is also a major constituent of subducting oceanic slabs. Lizardite dehydration temperature is also around 500°. This yields a remote normalized temperature of $\theta_\infty = -0.675$. We will use these values in the following calculations. From these dimensional parameters, we calculate the typical values of the nondimensional parameters, summarized on Table 3.

4. Linear Stability Analysis

[27] A stability analysis is performed to investigate whether the evolution in time of the pore pressure and temperature inside the shear zone remains bounded or not. The chemical reaction is active only for positive values of the normalized temperature a, so that unstable paths growing toward negative θ stop the reaction and the governing equations degenerate to the ones with no chemical effect (compare equation (38)). Thus a linear stability analysis gives us insights on the evolution of the temperature and pore pressure inside the shear zone when dehydration reactions are triggered. In particular we are interested in searching the conditions for which the reaction can destabilize the system.

4.1. Stability Condition

[28] The mathematical formulation is simplified by assuming linear diffusion profiles outside the shear zone. We investigate the behavior of the average temperature $\langle\theta\rangle$ and pressure $\langle\pi\rangle$ inside the shear zone. Following the approach of *Rudnicki and Chen* [1988] and *Segall and Rice* [1995], the pore pressure and temperature gradients are approximated by finite differences as

$$\frac{\partial \pi}{\partial y}\Big|_{y=0} = -\frac{\langle\pi\rangle - \pi_\infty}{l_{\mathrm{hy}}}, \tag{39}$$

$$\frac{\partial \theta}{\partial y}\Big|_{y=0} = -\frac{\langle\theta\rangle - \theta_\infty}{l_{\mathrm{th}}}, \tag{40}$$

where l_{hy} (l_{th}, respectively) is the normalized characteristic length of fluid (heat, respectively) diffusion. From these definitions, we get $l_{\mathrm{th}} = 1$ and $l_{\mathrm{hy}} = \sqrt{\alpha_{\mathrm{hy}} t^*/L} = \sqrt{\epsilon}$ because the characteristic time scale t^* is equal to the characteristic time of heat diffusion.

[29] By replacing the expression of u (equation (31)) into equalities (35) and (36), we obtain

$$\partial_t\langle\pi\rangle = \frac{1}{\mathcal{D}}\left[-\sqrt{\epsilon}\frac{\langle\pi\rangle - \pi_\infty}{\delta} + \left(\mathcal{P}^* + \mathcal{T}^*\right)\langle\theta\rangle - \frac{\langle\theta\rangle - \theta_\infty}{\delta} + (1 - \langle\pi\rangle)\frac{\mathcal{B}}{\delta}\right], \tag{41}$$

$$\partial_t\langle\theta\rangle = \frac{1}{\mathcal{D}}\Big[-\sqrt{\epsilon}(1-\mathcal{D})\frac{\langle\pi\rangle - \pi_\infty}{\delta}; + \left(\mathcal{T}^* + \mathcal{P}^*(1-\mathcal{D})\right)\langle\theta\rangle - \frac{\langle\theta\rangle - \theta_\infty}{\delta} + (1 - \langle\pi\rangle)\frac{\mathcal{B}}{\delta}\Big], \tag{42}$$

where

$$\mathcal{D} = 1 - \frac{\mathcal{AB}}{\delta}(1 - \langle\pi\rangle). \tag{43}$$

The above linear system of equations can be studied analytically. Linear stability analysis is classically performed around the stationary solution (fixed point of the mathematical system (41) and (42)) to investigate whether the fixed point is an attractor for the solution (i.e., the solution converges toward the stationary state) or a repulsor (i.e., the solution diverges) or a saddle point (i.e., attractor in one direction and repulsor in an other). As described in section 2.6, the amount of dehydrating minerals is assumed to be large enough so that the reaction kinetic is not limited by the finite quantity of reactant. Thus, the stationary solutions of equations (41) and (42) correspond to the initial trend at the onset of the reaction and cannot be extrapolated to infinitely long time scales. As we will show in section 5, using a finite amount of reactant does not dramatically change the conditions for instability, but rather modifies the long-term evolution of the perturbations.

[30] The stationary solution and the perturbation analysis are reported in detail in Appendix A. The steady state solution (π_0, θ_0) is expressed as

$$\pi_0 = \frac{\pi_\infty\sqrt{\epsilon}(1 - \mathcal{T}^*\delta) + \theta_\infty\mathcal{P}^*\delta + \mathcal{P}^*\mathcal{B}\delta}{\sqrt{\epsilon}(1 - \mathcal{T}^*\delta) + \mathcal{P}^*\mathcal{B}\delta}, \tag{44}$$

$$\theta_0 = \frac{\sqrt{\epsilon}(\theta_\infty + \mathcal{B}(1 - \pi_\infty))}{\sqrt{\epsilon}(1 - \mathcal{T}^*\delta) + \mathcal{P}^*\mathcal{B}\delta}. \tag{45}$$

Table 3. Typical Nondimensional Parameter Values for a Fault at 7 km Depth

Nondimensional Parameter	Symbol	Typical Value
Chemical pressurization parameter	$\mathcal{P}$*	10^{9} to 10^{10}
Chemical heat sink parameter	$\mathcal{T}$*	−10^{9} to −10^{10}
Pore pressure–slip rate coupling parameter	$\mathcal{A}$	3 × 10^{-4}
Shear heating parameter	$\mathcal{B}$	1
Fluid to heat diffusivity ratio	ϵ	10
Normalized slipping zone width	δ	10^{-6}
Normalized far field temperature	θ_∞	−0.675
Normalized far field pore pressure	π_∞	0.3

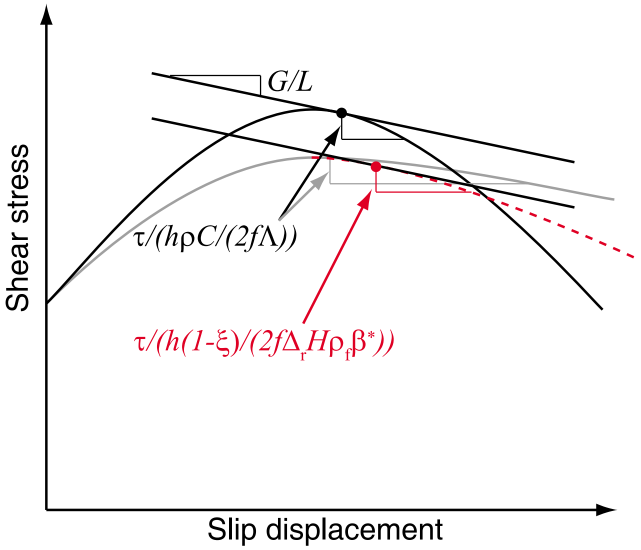

Figure 3. Schematic representation of the stability condition. Gray curve, stable case no reaction; black curve, unstable case no reaction; red dotted curve, unstable case with reaction.

The evolution in time of a small perturbation ($\langle\tilde{\pi}\rangle$, $\langle\tilde{\theta}\rangle$) around the stationary solution is given by

$$\begin{pmatrix} \langle\tilde{\pi}\rangle \\ \langle\tilde{\theta}\rangle \end{pmatrix} = c_1 e^{s_1 t}\mathbf{e}_1 + c_2 e^{s_2 t}\mathbf{e}_2, \tag{46}$$

where $c_{1,2}$ are arbitrary constants and $s_{1,2}$ and $\mathbf{e}_{1,2}$ are the eigenvalues and eigenvectors of the matrix, respectively:

$$\mathbf{G} = \frac{1}{\mathcal{D}}\begin{pmatrix} \frac{-\sqrt{\epsilon}-\mathcal{B}}{\delta} & \mathcal{P}^* + \mathcal{T}^* - \frac{1}{\delta} \\ \frac{\sqrt{\epsilon}(-1+\mathcal{D})-\mathcal{B}}{\delta} & \mathcal{P}^*(1-\mathcal{D}) + \mathcal{T}^* - \frac{1}{\delta} \end{pmatrix}. \tag{47}$$

The explicit form of $s_{1,2}$ and $\mathbf{e}_{1,2}$ is given by equations (A6) and (A7). The stability of the system is controlled by the sign of the eigenvalues. If at least one eigenvalue has a positive real part, the system is unstable. As shown in Appendix A, the stability condition is

$$\mathcal{D} > 0 \quad \text{and} \quad (1-\mathcal{D})\mathcal{P}^* + \mathcal{T}^* < \frac{1+\mathcal{B}+\sqrt{\epsilon}}{\delta}. \tag{48}$$

Condition (48) highlights the role of dehydration reactions on the stability of a fault, and thus on its seismic behavior. In the following we will investigate the physical meaning of condition (48) with reference to given geophysical situations.

4.2. Stability Fields

4.2.1. Without Reaction

[31] If we neglect the contribution of the chemical kinetic parameters $\mathcal{P}^*$ and $\mathcal{T}^*$, we can retrieve from equation (48) the solution derived by *Garagash and Rudnicki* [2003a]. The sign of parameter $\mathcal{D}$ fully determines the stability of the system. The expression of the dimensionless parameter $\mathcal{D}$ (equation (43)) can be rewritten using dimensional quantities as

$$\mathcal{D} = 1 - \frac{L}{G}\frac{\tau}{h\rho C/(2f\Lambda)}, \tag{49}$$

where τ is the current shear stress applied on the fault (equation (2)). From equation (49) we recognize the characteristic weakening distance for undrained, adiabatic slip $h\rho C/(2f\Lambda)$ [e.g., *Rice*, 2006]. Thus, the ratio $\tau/(h\rho C/(2f\Lambda))$ is the slope of the strength-slip curve of the fault, while G/L is the elastic stiffness of the crustal block. Negative $\mathcal{D}$ values correspond to $G/L < \tau/(h\rho C/(2f\Lambda))$, which means that the fault strength decreases more rapidly than the crustal block unloads (Figure 3, gray and black curves). This unstable behavior is identical to the well known frictional instability for slip weakening interfaces [e.g., *Scholz*, 2002]. The weakening mechanism is here triggered by thermal pore fluid pressurization.

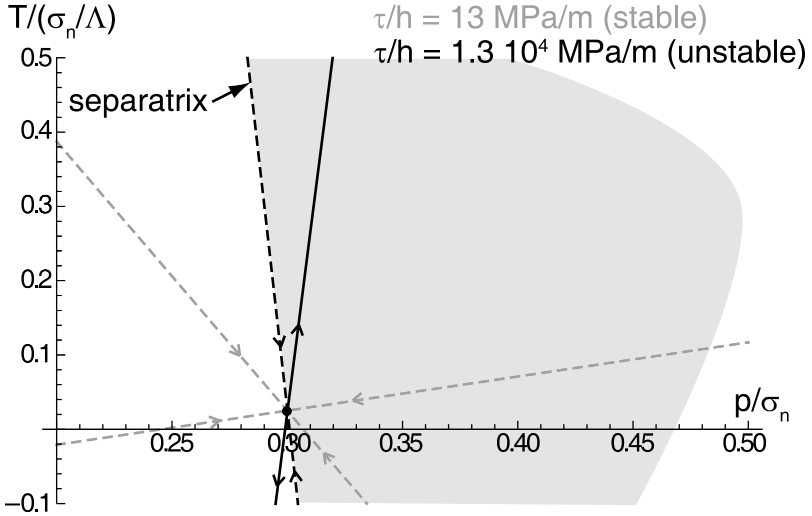

Figure 4. Eigenvectors and growth rates in a stable case (in gray for $\mathcal{A} = 3 \times 10^{-7}$) and an unstable case (in black for $\mathcal{A} = 3 \times 10^{-4}$) in the case of no reaction, i.e., $\mathcal{P}^* = \mathcal{T}^* = 0$. Other parameter values are reported on Table 3. The shaded area corresponds to perturbations that lead to slip acceleration.

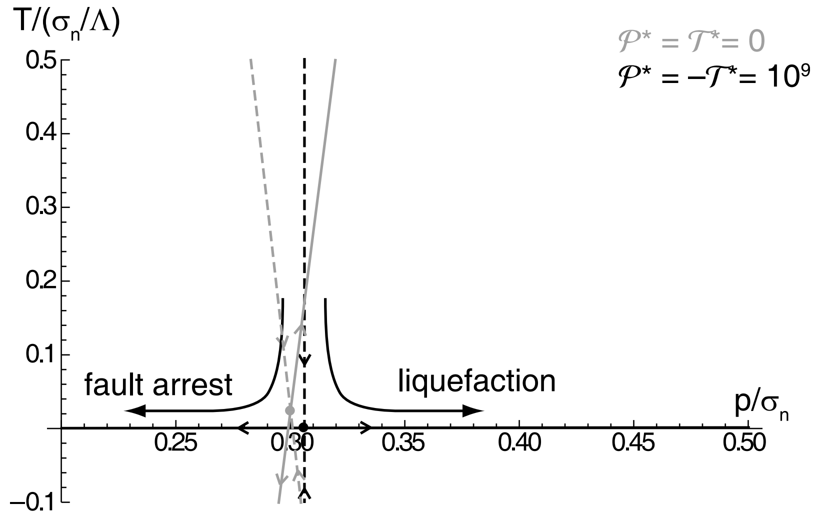

Figure 5. Linear stability diagram for the no reaction case (gray) and when dehydration occurs, $\mathcal{P}^* = -\mathcal{T}^* = 10^9$ (black). For both cases, $\mathcal{A} = 310^{-4}$. The solid line corresponds to the unstable eigendirection, and the dotted lines are stable eigendirections. The occurrence of the reaction induces either a rapid liquefaction (i.e., vanishing effective stress) or an arrest of the fault.

[32] Using the parameter values listed in Table 1, the block stiffness G/L is approximately 3 MPa m^{-1} and the ratio $\tau/(h\rho C/(2f\Lambda))$ is $\approx 0.2 \times \tau/h$. The stability is thus ensured when $\tau/h \lesssim 5 \times G/L \approx 15$ MPa m^{-1}, i.e., within highly pressurized fault zones. Similar critical shear stress value is obtained within the framework of rate-and-state friction laws, where the weakening mechanism arises from the intrinsic changes in friction coefficient [e.g., *Ruina*, 1983].

[33] A stable case ($\mathcal{D} > 0$) and an unstable case ($\mathcal{D} < 0$) are displayed in Figure 4 in the (π, θ) (or equivalently, the (p, T) plane). As expected from equations (44) and (45), the stationary solution is the same in both cases. If $\mathcal{D} > 0$, both eigenvalues are negative and any small perturbation from the stationary solution vanishes in time. For $\mathcal{D} < 0$, the stationary solution is unstable and is a saddle point. The eigenvector direction corresponding to the eigenvalue with negative real part acts as a separatrix in the (π, θ) plane, distinguishing between two regimes. If the small perturbation is a decrease in pressure or temperature, the instability grows toward lower pore pressure and temperature, thus stopping the fault motion. If the small perturbation is an increase in pore pressure or temperature, the instability grows toward high temperature and pore pressure, leading to an acceleration of the slip (shaded area on Figure 4). Interestingly, the slope of the unstable eigendirection is rather high, which means that the instability is mainly thermal for the set of parameters used.

4.2.2. Effect of the Reaction

[34] The role of the reaction is investigated using nonzero values of parameters $\mathcal{P}^*$ and $\mathcal{T}^*$. The stability condition (equation (48)) is then more restrictive compared to the case without reaction, as the second inequality $(1 - \mathcal{D})\,\mathcal{P}^* + \mathcal{T}^* < (1 + \mathcal{B} + \sqrt{\epsilon})/\delta$ must also be verified. The stability condition can be rewritten as

$$\mathcal{D} > \max\left\{0; 1 + \frac{\mathcal{T}^*}{\mathcal{P}^*} - \frac{1 + \mathcal{B} + \sqrt{\epsilon}}{\delta\mathcal{P}^*}\right\}. \tag{50}$$

We have seen previously how the condition $\mathcal{D} > 0$ could be interpreted as the ratio between the unloading stiffness of the medium and the weakening of the fault. Inequality 50 describes how the weakening behavior of the fault is affected by the occurrence of the dehydration reaction. Considering the parameter values listed in Table 3, the latter term $(1 + \mathcal{B} + \sqrt{\epsilon})/(\delta\ \mathcal{P}^*)$ can be neglected compared to 1. The stability condition becomes thus

$$\mathcal{D} \gtrsim \max\left\{0; 1 + \frac{\mathcal{T}^*}{\mathcal{P}^*}\right\}. \tag{51}$$

For the case $\mathcal{P}^* \leq -\mathcal{T}^*$, the pressurization induced by the release of water (chemical pressurization) is lower than the depressurization induced by the endothermic character of the reaction. The stability condition is thus unchanged and remains $\mathcal{D} > 0$. However, as we will show later, the evolution of the pore pressure and temperature in the unstable regime is dramatically different. Note that the condition (51) indicates that the dehydration process can never turn an unstable situation into a stable one.

[35] If $\mathcal{P}^* > -\mathcal{T}^*$, i.e., when the pore pressure increase due to the reaction is not fully compensated by the endothermic effect, the fault is unstable even when $\mathcal{D} > 0$, in the range $1 + \mathcal{T}^*/\mathcal{P}^* \gtrsim \mathcal{D} > 0$.

[36] In terms of dimensional quantities, inequality (51) can rewritten as

$$\frac{G}{L} \gtrsim \frac{\tau}{h(1-\xi)/\left(2f|\Delta_{\mathrm{r}}H_T|\rho_{\mathrm{f}}\beta^*\right)}, \tag{52}$$

which can be understood as the comparison between the unloading stiffness G/L and the slip weakening of the fault $\tau/(h(1-\xi)/(2f|\Delta_{\mathrm{r}}H_T|\rho_{\mathrm{f}}\beta^*))$ (Figure 3, red dotted curve). The quantity $h(1-\xi)/(2f|\Delta_{\mathrm{r}}H_T|\rho_{\mathrm{f}}\beta^*)$ is recognized as the equivalent slip weakening distance linked to the dehydration process, for undrained, adiabatic chemical pressurization [*Brantut et al.*, 2010, equation (23)].

[37] Interestingly, the approximate stability condition given by inequality (52) does not depend on the particular value of the kinetic parameter (dimensionless parameter c^*) that is loosely constrained by experimental data. The controlling factors are the enthalpy change of the reaction and the fluid mass release, that are well known for any particular dehydration reaction.

[38] Using the parameter values listed in Table 1, stability is ensured when $\tau/h \lesssim 0.3 \times G/L \approx 1$ MPa m^{-1}. This critical value is significantly lower than the value of 15 MPa m^{-1} determined in the absence of reaction (see previous section). Dehydration reactions are thus a destabilizing factor.

[39] The evolution of pore pressure and temperature in the fault zone at the onset of instability can be estimated graphically in the (π, θ) plane. Let us first consider the case $\mathcal{D} < 0$, i.e., unstable. Figure 5 represents the eigendirections for the case $\mathcal{P}^* = -\mathcal{T}^* = 0$ (no reaction) and for the case $\mathcal{P}^* = -\mathcal{T}^* = 10^9$ (with reaction). The stationary solution is very close to $\theta = 0$, i.e., $T = T_c$, and the pore pressure is slightly above the far field state. The relative evolution of pore pressure and temperature is significantly different from the case without reaction. The eigendirections tend to be perpendicular to each other, the unstable direction being almost parallel to the pore pressure axis. The instability evolves at almost constant temperature, very close to the dehydration temperature T_c. For a positive perturbation in pore pressure, the shear zone evolves toward vanishing effective normal stress while the temperature remains almost constant. For a negative perturbation in pore pressure, the unstable mode evolves toward the arrest of the fault. In nature, small perturbations of either signs are statistically encountered. Thus both situations can equally occur.

[40] In subsurface faults, the ambient temperature can be initially lower than the dehydration temperature. Shear heating can potentially trigger the onset of the dehydration reaction during the slip instability. In the following, we discuss how the subsequent evolution of the fault motion is controlled by the initial pore pressure. The stationary solution without the reaction is simply expressed as (equations (44) and (45))

$$\pi_0 = \pi_\infty, \tag{53}$$

$$\theta_0 = \theta_\infty + \mathcal{B}(1 - \pi_\infty). \tag{54}$$

If the initial pore pressure is greater than π_∞, the instability grows toward higher temperatures. Consequently, when the temperature reaches the threshold temperature of the reaction T_c, the new stationary state is given by equations (44) and (45). Considering that $\mathcal{T}^* \delta \gg 1$, π_0 can be expressed as

$$\pi_0 = \frac{-\pi_\infty \sqrt{\epsilon}\mathcal{T}^*/\mathcal{P} + \theta_\infty + \mathcal{B}}{\mathcal{B} - \sqrt{\epsilon}\mathcal{T}^*/\mathcal{P}}. \tag{55}$$

Using the parameter values listed in Table 1, the lower bound of the ratio $-\mathcal{T}^*/\mathcal{P}^*$ is of the order of 10^{-2}. It corresponds to a reaction that induces a large chemical pressurization (either because of high amount of released fluid and/or low solid volume change). The stationary pore pressure tends to

$$\lim_{\mathcal{T}^*/\mathcal{P}^* \to 0} \pi_0 = \pi_c = 1 + \frac{\theta_\infty}{\mathcal{B}}. \tag{56}$$

This limit value depends only on the boundary temperature θ_∞ and on the shear heating parameter $\mathcal{B}$. On the other hand, for high values of $-\mathcal{T}^*/\mathcal{P}^*$, the endothermic effect is dominant and the stationary pore pressure tends to π_∞ (i.e., identical to the no reaction case).

[41] If $\pi_c < \pi_\infty$, the sense of evolution of the perturbation is unchanged and the slip acceleration continues. If $\pi_c > \pi_\infty$ and $-\mathcal{T}^*/\mathcal{P}^*$ sufficiently small, the current state for the pore pressure at the onset of the reaction is lower than the new steady state pore pressure (with reaction), and the instability turns toward a slip arrest. This result is rather counterintuitive: although the chemical pressurization effect is large, the pore pressure actually decreases because the pressurization due to shear heating is stopped by the reaction. Conversely, for high values of $-\mathcal{T}^*/\mathcal{P}^*$ (high endothermic effect), the slip acceleration continues. This point is illustrated in Figure 6.

[42] In highly pressurized fault zones, the initial shear stress is low and the fault motion is stable in absence of reaction ($\mathcal{D} > 0$, Figure 7, light gray lines). As expected from inequality 51, the system is also stable when $\mathcal{P}^* = -\mathcal{T}^* = 10^9$ (Figure 7, dark gray lines). When $\mathcal{P}^* = -6\mathcal{T}^* = 6\ 10^9$, the system becomes highly unstable as both eigenvalues are positive. Note again the almost horizontal slopes in the pore pressure–temperature plot, which features an almost isothermal evolution of the instability.

[43] With dimensional quantities, the ratio $-\mathcal{T}^*/\mathcal{P}^*$ is written

$$\frac{-\mathcal{T}^*}{\mathcal{P}^*} = -\frac{\Delta_r H \Lambda}{\rho C} \frac{\rho_f \beta^*}{1 - \xi}. \tag{57}$$

The key control parameter is ξ, i.e., the ratio of the voids volume created by the reaction over the fluid volume released. Parameter ξ is strongly dependent on compaction processes during dehydration. Considering the high effective stress at depth, it is very likely that the pore space is partly compacted during the dehydration process. For porous rocks above a given effective pressure threshold, the solid matrix cannot sustain the stress and collapses, which is accompanied by a porosity decrease [e.g., *Wong et al.*, 1997, and references therein]. Recent experimental data on serpentinite deformed during dehydration [*Llana-Fúnez et al.*, 2007; *Rutter et al.*, 2009] also depict this type of behavior. In such cases, the value of ξ can be close to zero; that is, all the porosity created by the mineral dehydration can be simultaneously compacted. Then, the effect of the reaction on pore pressure is increased, and the system tends to be more unstable.

5. Numerical Examples

[44] In the previous section we have theoretically investigated the effect of dehydration reactions on the stability of a fault using representative values of the parameters. As mentioned earlier, the perturbation analysis focuses on the early times of the considered reaction as we have considered

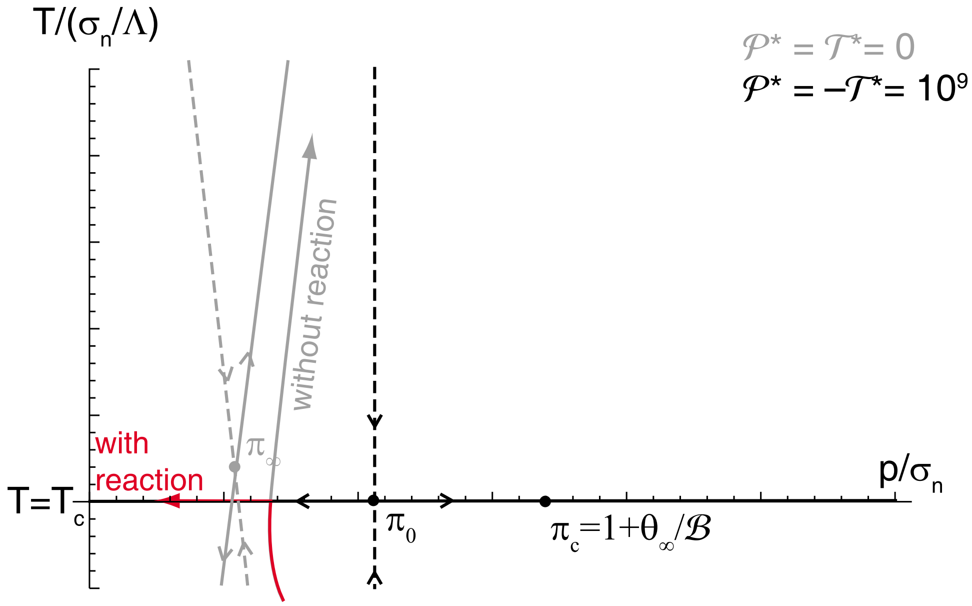

Figure 6. Schematic diagram showing how the sense of instability can be changed at the onset of the reaction. Here we have $\pi_c > \pi_\infty$. The instability is initially supposed to lead to a slip acceleration (when no reaction occurs), but when the system reaches the threshold temperature T_c, the instability changes sign and leads to an arrest of the fault motion.

a linear form for the kinetic law ($\mu \ll 1$). This approach allowed us to investigate the instability regimes. We can relax these assumptions and develop a numerical solution for the pore pressure and temperature inside the band (equations (35) and (36)), using expressions 39 and 40 for the pore pressure and temperature gradients at the boundary of the shear band, and the Arrhenius law (equation (34)) for the reaction progress.

[45] First the case $\mathcal{D} < 0$ is investigated. The parameters are set as follows: $\mathcal{A} = 3\ 10^{-4}$, $p_\infty = 70$ MPa and $T_\infty = 210$°C, corresponding to conditions at midseismogenic depth (see Table 3). In the case of no reaction, if the initial pressure p_0 is less than the far field (steady state) pressure p_∞, the instability tends to stop the fault motion (Figure 8, gray curve). Conversely, if $p_0 > p_\infty$ then the instability is an acceleration of the fault motion (Figure 8, solid black curve). In all cases, the pore pressure does not vary far from its initial value, whereas the temperature change is very significant. This thermal runaway is consistent with the analytical results detailed in the previous section.

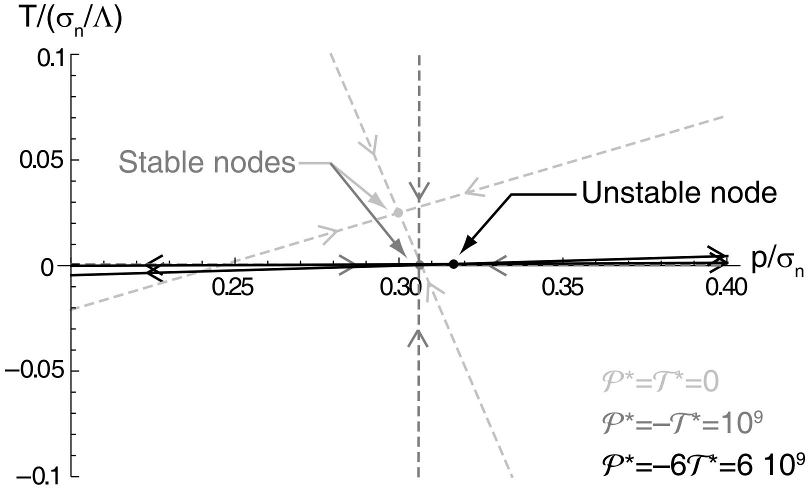

Figure 7. Linear stability diagram for the no reaction case (light gray) and various values of kinetic parameters. For all cases, $\mathcal{A} = 3 10^{-7}$, i.e., a normally stable situation. The solid lines correspond to unstable eigendirections, and the dotted lines are stable eigendirections. If no reaction occurs or if $\mathcal{P}^* = -\mathcal{T}^*$, the system is stable. If $\mathcal{P}^*$ is significantly higher than $\mathcal{T}^*$, both eigendirections become unstable. Note that in the latter case, the evolution of the system is almost isothermal.

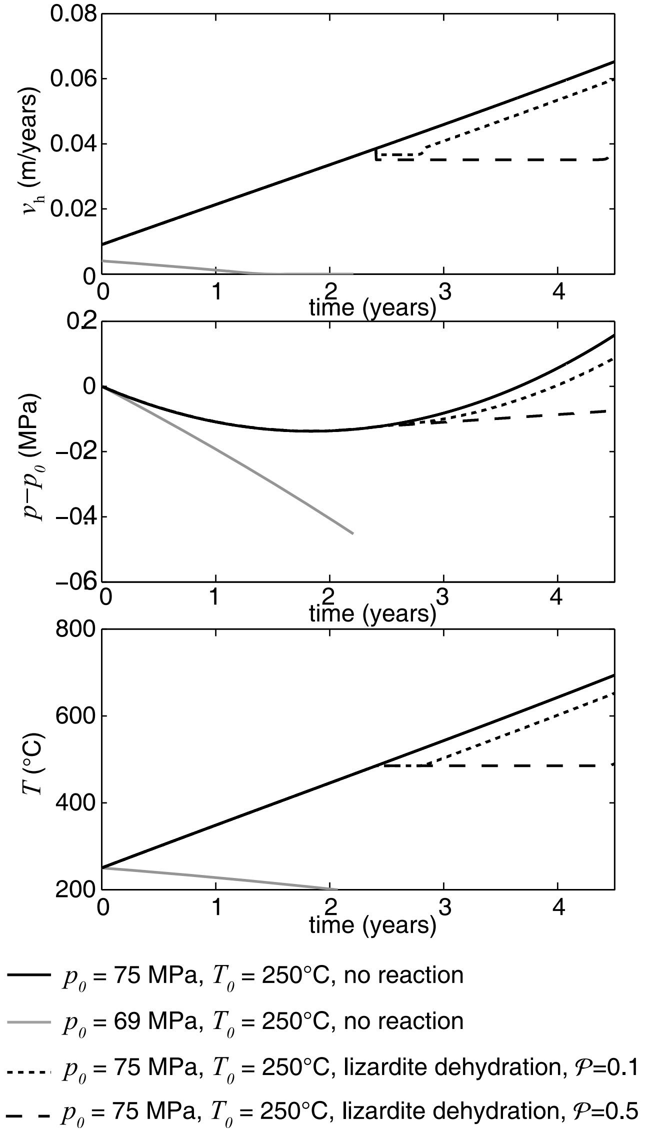

Figure 8. Slip velocity, pore pressure, and temperature evolution for various initial conditions in the case $\mathcal{D} < 0$. The dehydration of lizardite is implemented by using the Arrhenius law (equation (28)), and the parameters reported in Table 2. Slip acceleration is stopped during the reaction; that is, the higher value of $\mathcal{P}$, the longer it stops. The higher value $\mathcal{P} = 0.5$ corresponds to a large compaction, i.e., assuming $\xi = 0$.

[46] This situation can change when the reaction is activated. Here we considered lizardite dehydration at 485°C, using the kinetic parameters reported in Table 2. In this case, the steady state pore pressure is higher than p_∞ (see for instance equation (A4)). The fault acceleration is stopped when the reaction occurs, and starts again when the reaction is completed (Figure 8, dotted black curve). The duration of the stabilization of the slip is controlled by the parameter $\mathcal{P}$, i.e., the amount of dehydrating mineral (parameter m_0) and the change in pore volume ξ.

[47] The case $\mathcal{D} > 0$ can also be investigated. It would correspond to a combination of a high stiffness G/L, a relatively large slipping zone width h and/or a low thermal pressurization factor Λ. The parameter values used to model such a situation are the same as those presented in Table 1, except that $G = 50 \times 10^9$ Pa, $L = 10^3$ m, $h = 10^{-1}$ m, and $\Lambda = 0.3 \times 10^6$ MPa/°C. Note that such values remain in a plausible range for natural fault rocks. One important parameter is the ratio G/L, which is however loosely constrained considering the oversimplification of the fault geometry. An extension of our model to two or three dimensions could help to obtain a more realistic configuration and thus estimate a realistic range for the unloading stiffness of the crustal block.

[48] When no reaction occurs, the system is stable. However, the dehydration reaction induces a transient instability that ends when the reaction is finished (Figure 9). It consists in an acceleration of the fault motion up to 8 meters per year, 2 orders of magnitude above the remote loading rate. In this case, the pore pressure increase is only due to the chemical effect: the system undergoes a chemical pressurization. The pore pressure peak will thus be high for large values of $\mathcal{P}$, for instance if ξ is low (e.g., if compaction occurs).

[49] The case $\mathcal{D} > 0$ can be further studied in the setting of a deep fault embedded in serpentinite, e.g., within a subduction zone. The parameter values used in this situation are summarized in Table 4. The depth is 35 km, which corresponds to a lithostatic pressure of the order of 1 GPa. In the case of a highly pressurized medium, we assume an ambient pore pressure of 920 MPa. The ambient initial temperature is set at 500°C to simulate a cold geothermal gradient (i.e., 15 °C km^{-1}). The inital mass of water that can be released by the dehydration of serpentine per unit volume is m_0 = 400 kg m^{-3} (see section 3). Here again, we use $G = 50 \times 10^9$ Pa, $L = 10^3$ m, $h = 10^{-1}$ m, and $\Lambda = 0.3 \times 10^6$ Pa °C to model astable fault motion in absence of reaction.

[50] Recalling the expression of the slip velocity, obtained by combining equations (31) and (35)

$$u = \frac{1}{\mathcal{D}}\left(1 + \frac{\mathcal{A}}{\delta}\left(\sqrt{\epsilon}(\pi_\infty - \pi) + (\theta_\infty - \theta) + \delta(\mathcal{T} + \mathcal{P})\partial_t\mu\right)\right), \tag{58}$$

an estimate of the change of velocity Δu at the onset of the reaction is given by

$$\Delta u = \frac{\mathcal{A}}{\mathcal{D}}(\mathcal{T} + \mathcal{P})\partial_t\mu. \tag{59}$$

In the example shown in Figure 10, we show that when the reaction starts, the slip velocity suddenly increases up to 3.6 m year^{-1}, and then decreases rapidly to the initial value. The crisis lasts ~4 days. This increase is mainly controlled by the value of the dimensionless parameter $\mathcal{P}$. From the estimate of the velocity, it is possible to obtain the total slip Δd associated with the onset of the reaction:

$$\Delta d = \frac{\mathcal{A}}{\mathcal{D}}(\mathcal{T} + \mathcal{P})\Delta\mu, \tag{60}$$

where $\Delta\mu$ is the increment of reaction progress during the transient. The slip history is thus entirely dictated by the reaction progress. The larger amount of dehydrating mineral, the larger the slip is. The magnitude M of the slip event for a

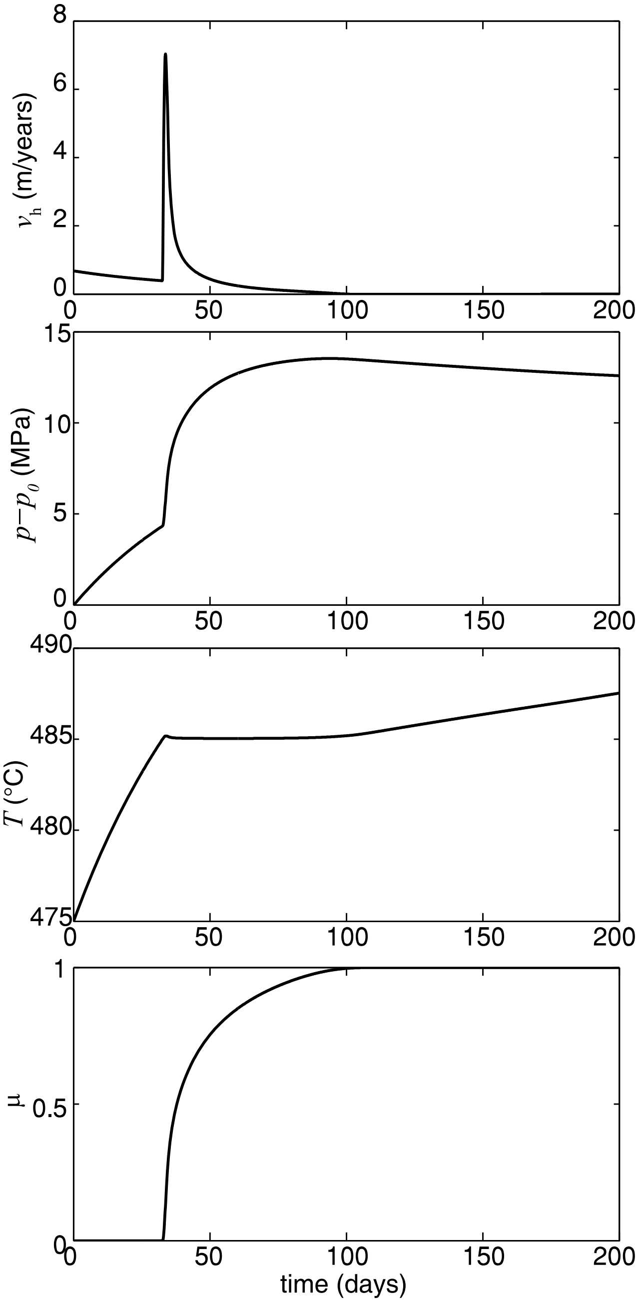

Figure 9. Slip velocity, pore pressure, and temperature evolution in the case $\mathcal{D} > 0$ (stable without reaction). The dehydration reaction induces a transient increase in pore pressure, temperature, and slip velocity. The slip acceleration is fast at the onset of the reaction and then decelerates. The total duration of the slip event is a few days.

given fault surface S is thus

$$M = G(\Delta d)S \propto \Delta\mu. \qquad (61)$$

The scaling given by equation (61) implies that the finite amount of dehydrating mineral dictates the size of the slow slip event. The moment rate is controlled by the reaction kinetic.

6. Conclusions

[51] A one-dimensional spring-slider block model has been used to analyze the instabilities emerging from thermal pressurization and mineral dehydrations within a shear zone. The stability condition has been derived analytically, and represented in terms of critical stiffness of the fault zone. Instabilities arise from two distinct origins: (1) from the thermal pressurization process itself, associated with a critical stiffness equal to $\tau/(h\rho C/2f\ \Lambda)$, and (2) from the dehydration reactions associated with a critical stiffness equal to $\tau/(h(1-\xi)/(2f|\Delta_r H_T|\rho_f\beta^*))$.

[52] The instabilities originated from thermal pressurization (type 1) can lead either to an arrest or to an unbounded acceleration of the fault motion, depending on the sign of the perturbation. Such instabilities are themselves modified by the occurrence of the reaction. In the analytical approach, assuming an infinite amount of dehydrating mineral, the instability develops toward vanishing effective normal stress while the temperature remains close to the dehydration temperature. The numerical tests performed with a finite amount of dehydrating mineral demonstrate that this effect is actually limited in time, and stops when the reaction is completed. The numerical tests showed that the linearization of the Arrhenius law is a good approximation, as the temperature never rises much higher than the equilibrium temperature.

[53] For sufficiently small shear stress values, of the order of a few MPa, instabilities linked to thermal pressurization are excluded. However, instabilities can still arise from the dehydration reactions (type 2), as the corresponding critical stiffness is higher. Numerical simulations show that such instabilities tend to lead to a transient acceleration of the fault motion. The acceleration stops when the reaction is finished. The maximum slip rate is of the order of a few meters per year during the transient. The magnitude of such events is dictated by the amount of dehydrating mineral, and the moment rate is dictated by the reaction kinetic. The transients slow slip events could correspond to slow and

Table 4. Parameters Used for the Calculation of a Slip on a Serpentine-Bearing Fault at 35 km Depth

Physical Parameter	Symbol	Value	Unit
Size of the crustal block	L	10^3	m
Elastic stiffness of the crustal block	G	$50\ 10^9$	Pa
Normal stress	σ_n	10^9	Pa
Mass of released fluid	m_0	400	kg m^{-3}
Width of the slipping zone	h	10^{-1}	m
Far field pore pressure	p_∞	92010^6	Pa
Far field temperature	T_∞	500	°C
Heat diffusivity	α_{th}	10^{-6}	$m^2\ s^{-1}$
Fluid diffusivity	α_{hy}	10^{-6}	$m^2\ s^{-1}$
Thermal pressurization factor	Λ	$0.3\ 10^6$	Pa $C^{\circ -1}$
Enthalpy of the reaction	$\lvert\Delta_r H_T\rvert$	500	kJ kg^{-1}
Void creation vs fluid release ratio	ξ	0.8	
Fluid to heat diffusivity ratio	ϵ	1	
Normalized slipping zone width	δ	$5\ 10^{-5}$	
Chemical pressurization parameter	$\mathcal{P}$	0.032	
Chemical heat sink parameter	$\mathcal{T}$	−0.022	
Shear heating parameter	$\mathcal{B}$	0.056	
Elastic coupling parameter	$\mathcal{A}$	0.01	

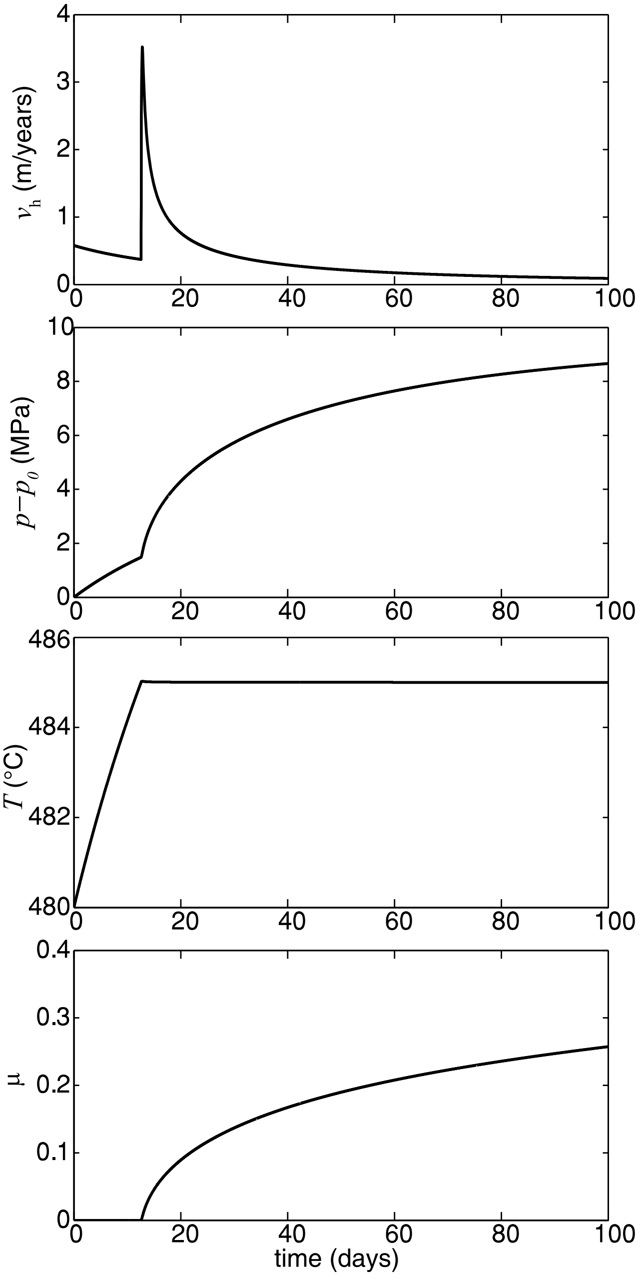

Figure 10. Fault at 35 km depth: Slip velocity, pore pressure, and temperature evolution in the case $\mathcal{D} > 0$ (stable without reaction) and for parameters detailed in Table 4. The onset of dehydration is marked by a transient increase of temperature and slip velocity. This transient event lasts ~2 days. The fault motion remains otherwise stable.

silent slip events detected in several subduction zones. Recent studies [*Melbourne and Webb*, 2003; *Rogers and Dragert*, 2003] have shown that slow earthquakes, slip transients, and low-frequency earthquakes are generally associated with nonvolcanic tremor activity in subduction zones. On the other hand, *Burlini et al.* [2009] have recently shown that the tremor signals recorded in the field could be qualitatively compared to the acoustic signals recorded in the laboratory during serpentinite dehydration. These observations, when combined with our study, suggest that nonvolcanic tremors, if indeed linked to dehydration reactions occurring within the subducting slab, could be accompanied by slip transients. In fact, both seem to result from the same single phenomenon: dehydration reactions in the subducting oceanic crust.

[54] In our model, the stability of fault motion is ensured when the shear stress acting on the fault is extremely low (a few MPa) (see equation (52)). In similar one dimensional fault zone models that use the empirical rate-and-state friction law as a constitutive equation for the evolution of friction at the interface, the stability condition is written as [e.g., *Ruina*, 1983]

$$G/L > (\sigma_\mathrm{n} - p)(b - a)/d_c, \qquad (62)$$

where a, b and d_c are constitutive parameters of the interface. Using typical values of $(b - a) = 0.005$, $d_c = 10^{-2}$ m [e.g., *Segall and Rice*, 1995], and $G/L = 3$ MPa m^{-1}, the stability condition is $(\sigma_n - p) < 6$ MPa. Such a value is of the same order of magnitude as the one found in our model. Thus, the instability expected within the rate-and-state framework arises at similar conditions as the instability determined in a dehydrating fault zone. However, a comprehensive analysis incorporating both fluid pressurization, dehydration and rate-and-state friction should be performed in order to compare the various effects in a single framework.

[55] Throughout this study, the calculations and numerical simulations always showed a strong thermal effect of the dehydration reaction. The dynamic change in pore pressure due to shear heating explains partly the almost isothermal behavior of the shear zone, but the most important cause is the fact that dehydration reactions are endothermic. This is consistent with previous studies of rapid fault slip including endothermic chemical reactions [*Sulem and Famin*, 2009; *Brantut et al.*, 2010, 2011], that emphasized this strong thermal effect even at slip velocities as high as 1 m s^{-1}. The initial amount of hydrous mineral is a key parameter. After an earthquake, this amount can be strongly depleted and the thermal effect can be lost over the seismic cycle. However, if the rupture passes through another part of the fault zone, even a few centimeters far from the previous slip zone, the amount of minerals to dehydrate is intact. Moreover, the almost ubiquitous presence of clay minerals along major fault zones [*Sulem et al.*, 2004; *Solum et al.*, 2006; *Hirono et al.*, 2008] may suggest interseismic fluid circulations and alteration of gouge zones to form a significant amount of unstable, hydrous minerals.

[56] The reaction kinetic was described by a simple first-order reaction rate and an Arrhenius law to account for its temperature dependency. A more detailed investigation would also include the pore pressure dependency of the reaction rate. Qualitatively, an increase in pore pressure should induce a decrease of the reaction rate. Such a negative feedback could hamper the growth of instabilities. In the lack of quantitative experimental data on the effect of pore pressure on the kinetic law of dehydration reactions, this effect was not considered in our analysis. Nevertheless, it is likely that the pore pressure variations have a second-order effect on reaction kinetics, compared to the major temperature dependency dictated by the Arrhenius law. Indeed, variations in pore pressure may affect the equilibrium conditions of the reactions, and merely offset the dehydration temperatures.

Thorough experimental work would be needed to quantify this effect so that it can be implemented in our model.

[57] In this study we only investigated nucleation by shear heating and pore fluid pressurization. A more complete description would include rate and state dependency of the friction coefficient, dilatancy or compaction. *Segall and Rice* [2006] have shown that thermal pressurization plays a role only at a late phase of nucleation. Metamorphic dehydration reactions may have important effects even at early times, if the ambient temperature is already close to the equilibrium temperature of these reactions. The exact interplay of metamorphism and earthquake nucleation is thus still an open question.

[58] We have analyzed the case of endothermic dehydration reactions with positive total volume change. However, one should bear in mind that at greater depth, several endothermic reactions with negative volume change, such as eclogitization and/or olivine to spinel transitions, take place. Although these reactions involve no or little fluid phase, the stability analysis of a medium undergoing such transitions could be an interesting future perspective, which might once again highlight the importance of metamorphism in earthquake nucleation.

Appendix A: Explicit Expressions of the Perturbation

[59] In this section we present a linearized stability analysis of the system formed by equations (41) and (42). Such a system can be written in matrix form as follows:

$$\partial_t \mathbf{x} = \mathbf{G}\mathbf{x} + \mathbf{c}, \tag{A1}$$

where $\mathbf{x} = (\langle\pi\rangle, \langle\theta\rangle)$,

$$\mathbf{G} = \frac{1}{\mathcal{D}} \begin{pmatrix} \frac{-\sqrt{\epsilon}-\mathcal{B}}{\delta} & \mathcal{P}^* + \mathcal{T}^* - \frac{1}{\delta} \\ \frac{\sqrt{\epsilon}(-1+\mathcal{D})-\mathcal{B}}{\delta} & \mathcal{P}^*(1-\mathcal{D}) + \mathcal{T}^* - \frac{1}{\delta} \end{pmatrix}, \tag{A2}$$

and

$$\mathbf{c} = \frac{1}{\delta\mathcal{D}} \begin{pmatrix} \sqrt{\epsilon}\pi_\infty + \theta_\infty + \mathcal{B} \\ (1-\mathcal{D})\sqrt{\epsilon}\pi_\infty + \theta_\infty + \mathcal{B} \end{pmatrix}. \tag{A3}$$

[60] The stationary solutions of the system, i.e., $\mathbf{x}_0 = (\pi_0, \theta_0)$ verifying $\mathbf{G}\mathbf{x}_0 + \mathbf{c} = 0$, is

$$\pi_0 = \frac{1}{\sqrt{\epsilon}\left(1-\mathcal{T}^*\delta\right) + \mathcal{P}^*\mathcal{B}\delta} \times \left(\pi_\infty\sqrt{\epsilon}\left(1-\mathcal{T}^*\delta\right) + \theta_\infty\mathcal{P}^*\delta + \mathcal{P}^*\mathcal{B}\delta\right), \tag{A4}$$

$$\theta_0 = \frac{1}{\sqrt{\epsilon}\left(1-\mathcal{T}^*\delta\right) + \mathcal{P}^*\mathcal{B}\delta}\left(\sqrt{\epsilon}(\theta_\infty + \mathcal{B}(1-\pi_\infty))\right). \tag{A5}$$

[61] Assuming that the system is at steady state, we study the evolution in time of a small perturbation $\tilde{\mathbf{x}} = (\langle\tilde{\pi}\rangle, \langle\tilde{\theta}\rangle)$. This perturbation verifies $\partial_t\tilde{\mathbf{x}} = \mathbf{G}\tilde{\mathbf{x}}$. The eigenvalues of matrix $\mathbf{G}$ are

$$s_{1,2} = \frac{1}{2\mathcal{D}}\left[-\frac{1+\mathcal{B}+\sqrt{\epsilon}}{\delta} + (1-\mathcal{D})\mathcal{P}^* + \mathcal{T}^* \pm \sqrt{\left(-\frac{1+\mathcal{B}+\sqrt{\epsilon}}{\delta} + (1-\mathcal{D})\mathcal{P}^* + \mathcal{T}^*\right)^2 + 4\frac{\mathcal{D}}{\delta^2}\left(-\sqrt{\epsilon} - \left(\mathcal{P}^*\mathcal{B} - \mathcal{T}^*\sqrt{\epsilon}\right)\delta\right)}\right], \tag{A6}$$

respectively, and the corresponding eigenvectors are

$$\mathbf{e}_{1,2} = \left(\frac{\delta}{\sqrt{\epsilon}(1-\mathcal{D}) + \mathcal{B}}\left[(1-\mathcal{D})\mathcal{P}^* + \mathcal{T}^* - \frac{1}{\delta} - s_{1,2}\mathcal{D}\right], 1\right), \tag{A7}$$

respectively. The solution is thus

$$\tilde{\mathbf{x}} = c_1 e^{s_1 t}\mathbf{e}_1 + c_2 e^{s_2 t}\mathbf{e}_2, \tag{A8}$$

where $c_{1,2}$ are arbitrary constants. The perturbation will thus grow exponentially in time if at least one of the eigenvalues $s_{1,2}$ is positive, i.e., $\mathrm{Re}(s_{1,2}) > 0$.

[62] If $\mathcal{D} < 0$, then s_2 is always positive while s_1 remains negative, independently from the values of $\mathcal{P}^*$ and $\mathcal{T}^*$. The system is unstable and corresponds to a saddle point (see example in Figure 4). All the perturbations lying on the left of the separatrix follow the unstable direction toward decreasing temperature and pressure. Conversely, those lying on the right of the separatrix follow the unstable eigendirection toward increasing temperature and pressure.

[63] If $\mathcal{D} > 0$, positive eigenvalues can be found when

$$(1-\mathcal{D})\mathcal{P}^* + \mathcal{T}^* > \frac{1+\mathcal{B}+\sqrt{\epsilon}}{\delta}. \tag{A9}$$

Notation

u normalized slip velocity.
π normalized pore pressure.
θ normalized temperature.
m_0 total mass of releasable water per unit of rock mass.
ξ ratio of the volume of voids created over the volume of fluid released per unit of reaction progress.
$\mathcal{P}$ nondimensional pore pressure increase per unit of reaction progress (chemical pressurization effect).
$\mathcal{T}$ nondimensional temperature change per unit of reaction progress (endothermic effect of the reaction).
$\mathcal{P}^*$ chemical pressurization effect including the temperature dependency of the reaction kinetic.
$\mathcal{T}^*$ endothermic effect including the temperature dependency of the reaction kinetic.

$\mathcal{A}$ nondimensional coupling between pore pressure rate and slip velocity.
$\mathcal{B}$ nondimensional frictional heating source.
ϵ ratio of hydraulic diffusivity over heat diffusivity.
δ dimensionless thickness of the localized shear zone.

[64] **Acknowledgments.** The authors thank Fabrice Brunet for fruitful discussions and two anonymous reviewers for their useful comments. N.B. gratefully thanks Basile Gallet for his help on the stability analysis.

References

Brantut, N., A. Schubnel, J.-N. Rouzaud, F. Brunet, and T. Shimamoto (2008), High-velocity frictional properties of a clay-bearing fault gouge and implications for earthquake mechanics, *J. Geophys. Res.*, *113*, B10401, doi:10.1029/2007JB005551.

Brantut, N., A. Schubnel, J. Corvisier, and J. Sarout (2010), Thermochemical pressurization of faults during coseismic slip, *J. Geophys. Res.*, *115*, B05314, doi:10.1029/2009JB006533.

Brantut, N., R. Han, T. Shimamoto, N. Findling, and A. Schubnel (2011), Fast slip with inhibited temperature rise due to mineral dehydration: Evidence from experiments on gypsum, *Geology*, in press.

Burlini, L., G. Di Toro, and P. Meredith (2009), Seismic tremor in subduction zones: Rock physics evidence, *Geophys. Res. Lett.*, *36*, L08305, doi:10.1029/2009GL037735.

Chester, F. M. (1994), Effects of temperature on friction: Constitutive equations and experiments with quartz gouge, *J. Geophys. Res.*, *99*, 7247–7261.

Chester, J. S., F. M. Chester, and A. K. Kronenberg (2005), Fracture surface energy of the Punchbowl fault, San Andreas system, *Nature*, *437* (1), 133–136.

Dietrich, J. H. (1978), Time-dependent friction and mechanics of stick-slip, *Pure Appl. Geophys.*, *116*, 790–806.

Dietrich, J. H. (1979), Modeling of rock friction: 1. Experimental results and constitutive equations, *J. Geophys. Res.*, *84*, 2161–2168.

Garagash, D. I., and J. W. Rudnicki (2003a), Shear heating of a fluid-saturated slip-weakening dilatant fault zone: 1. Limiting regimes, *J. Geophys. Res.*, *108*(B2), 2121, doi:10.1029/2001JB001653.

Garagash, D. I., and J. W. Rudnicki (2003b), Shear heating of a fluid-saturated slip-weakening dilatant fault zone: 2. Quasi-drained regime, *J. Geophys. Res.*, *108*(B2), 2472, doi:10.1029/2002JB002218.

Ghabezloo, S., and J. Sulem (2009), Stress-dependent thermal pressurization of a fluid-saturated rock, *Rock Mech. Rock Eng.*, *42*(1), 1–24.

Goren, L., E. Aharonov, and M. H. Anders (2010), The long runout of the Heart Mountain landslide: Heating, pressurization, and carbonate decomposition, *J. Geophys. Res.*, *115*, B10210, doi:10.1029/2009JB007113.

Hamada, Y., T. Hirono, W. Tanikawa, W. Soh, and S. Song (2009), Energy taken up by co-seismic chemical reactions during a large earthquake: An example from the 1999 Taiwan Chi-Chi earthquake, *Geophys. Res. Lett.*, *36*, L06301, doi:10.1029/2008GL036772.

Heard, H. C., and W. W. Rubey (1966), Tectonic implications of gypsum dehydration, *Geol. Soc. Am. Bull.*, *77*, 741–760.

Hirono, T., et al. (2008), Clay mineral reactions caused by frictional heating during an earthquake: An example from the Taiwan Chelungpu fault, *Geophys. Res. Lett.*, *35*, L16303, doi:10.1029/2008GL034476.

Lee, T. C., and P. T. Delaney (1987), Frictional heating and pore pressure rise due to fault slip, *Geophys. J. R. Astron. Soc.*, *88*, 569–591.

Llana-Fúnez, S., K. H. Brodie, E. H. Rutter, and J. C. Arkwright (2007), Experimental dehydration kinetics of serpentinite using pore volumometry, *J. Metamorph. Geol.*, *25*, 423–438.

Marone, C. (1998), Laboratory-derived friction laws and their application to seismic faulting, *Annu. Rev. Earth Planet. Sci.*, *26*, 643–696.

Marone, C., C. B. Raleigh, and C. H. Scholz (1990), Frictional behavior and constitutive modeling of simulated fault gouge, *J. Geophys. Res.*, *95*, 7007–7025.

Melbourne, T. I., and F. H. Webb (2003), Slow but not quite silent, *Science*, *300*, 1886–1887.

Milsch, H., and C. H. Scholz (2005), Dehydration-induced weakening and fault slip in gypsum: Implications for the faulting process at intermediate depth in subduction zones, *J. Geophys. Res.*, *110*, B04202, doi:10.1029/2004JB003324.

Mizoguchi, K. (2005), High-velocity frictional behavior of Nojima fault gouge and its implications for seismogenic fault motion, Ph.D. thesis, Kyoto Univ., Kyoto, Japan.

Murrell, S. A. F., and I. A. H. Ismail (1976), The effect of decomposition of hydrous minerals on the mechanical properties of rocks, *Tectonophysics*, *31*, 207–258.

Noda, H., and T. Shimamoto (2005), Thermal pressurization and slip-weakening distance of a fault: An example of Hanaore fault, southwest Japan, *Bull. Seismol. Soc. Am.*, *95*(4), 1224–1233.

Olgaard, D. L., S.-C. Ko, and T.-F. Wong (1995), Deformation and pore pressure in dehydrating gypsum under transiently drained conditions, *Tectonophysics*, *245*, 237–248.

Raleigh, C. B., and M. S. Paterson (1965), Experimental deformation of serpentinite and its tectonic implications, *J. Geophys. Res.*, *70*, 3965–3985.

Rempel, A., and J. R. Rice (2006), Thermal pressurization and onset of melting in fault zones, *J. Geophys. Res.*, *111*, B09314, doi:10.1029/2006JB004314.

Rice, J. R. (2006), Heating and weakening of faults during earthquake slip, *J. Geophys. Res.*, *111*, B05311, doi:10.1029/2005JB004006.

Robie, R. A., B. S. Hemingway, and J. R. Fisher (1979), Thermodynamic properties of minerals and related substances at 298.15 K and 1 bar (10^5 pascals) pressure and at higher temperatures, *U.S. Geol. Surv. Bull.*, *1452*.

Rogers, G., and H. Dragert (2003), Episodic tremor and slip on the Cascadia subduction zone: The chatter of silent slip, *Science*, *300*, 1942–1943.

Rosakis, P., A. J. Rosakis, G. Ravichandran, and J. Hodowany (2000), A thermodynamic internal variable model for the partition of plastic work into heat and stored energy in metals, *J. Mech. Phys. Solids*, *48*, 581–607.

Rudnicki, J. W., and C.-H. Chen (1988), Stabilization of rapid frictional slip on a weakening fault by dilatant hardening, *J. Geophys. Res.*, *93*, 4745–4757.

Ruina, A. L. (1983), Slip instability and state variable friction laws, *J. Geophys. Res.*, *88*, 10,359–10,370.

Rutter, E. H., S. Llana-Fùnez, and K. H. Brodie (2009), Dehydration and deformation of intact cylinders of serpentinite, *J. Struct. Geol.*, *31*, 29–43, doi:10.1016/j.jsg.2008.09.008.

Saikia, N., P. Sengupta, P. K. Gogoi, and P. C. Borthakur (2002), Kinetics of dehydroxylation of kaolin in presence of oil field effluent treatment plant sludge, *Appl. Clay Sci.*, *22*, 93–102.

Scholz, C. H. (2002), *The Mechanics of Earthquake and Faulting*, 2nd ed., Cambridge Univ. Press, Cambridge, U. K.

Segall, P., and J. R. Rice (1995), Dilatancy, compaction, and slip instability of a fluid-infiltrated fault, *J. Geopys. Res.*, *100*, 22,155–22,171.

Segall, P., and J. R. Rice (2006), Does shear heating of pore fluid contribute to earthquake nucleation?, *J. Geophys. Res.*, *111*, B09316, doi:10.1029/2005JB004129.

Solum, L. G., S. H. Hickman, D. A. Lockner, D. E. Moore, B. A. van der Pluijm, A. M. Schleicher, and J. P. Evans (2006), Mineralogical characterization of protolith and fault rocks from the SAFOD main hole, *Geophys. Res. Lett.*, *33*, L21314, doi:10.1029/2006GL027285.

Sulem, J., and V. Famin (2009), Thermal decomposition of carbonates in fault zones: Slip-weakening and temperature-limiting effects, *J. Geophys. Res.*, *114*, B03309, doi:10.1029/2008JB006004.

Sulem, J., I. Vardoulakis, H. Ouffroukh, M. Boulon, and J. Hans (2004), Experimental characterization of the thermo-poro-mechanical properties of the Aegion fault gouge, *C. R. Geosci.*, *336*(4–5), 455–466.

Sulem, J., P. Lazar, and I. Vardoulakis (2007), Thermo-poro-mechanical properties of clayey gouge and application to rapid fault shearing, *Int. J. Numer. Anal. Methods Geomech.*, *31*, 523–540.

Suzuki, T., and T. Yamashita (2006), Nonlinear thermoporoelastic effects on dynamic earthquake rupture, *J. Geophys. Res.*, *111*, B03307, doi:10.1029/2005JB003810.

Suzuki, T., and T. Yamashita (2007), Understanding of slip-weakening and -strengthening in a single framework of modeling and its seismological implications, *Geophys. Res. Lett.*, *34*, L13303, doi:10.1029/2007GL030260.

Veveakis, E., S. Alevizos, and I. Vardoulakis (2010), Chemical reaction capping of thermal instabilities during shear of frictional faults, *J. Mech. Phys. Solids*, *58*, 1175–1194.

Wibberley, C. A. J. (2002), Hydraulic diffusivity of fault gouge zones and implications for thermal pressurization during seismic slip, *Earth Planets Space*, *54*, 1153–1171.

Wibberley, C. A. J., and T. Shimamoto (2003), Internal structure and permeability of major-lip fault zones: The Median Tectonic Line in Mie Prefecture, southwest Japan, *J. Struct. Geol.*, *25*, 59–78.

Wong, T. F., C. David, and W. Zhu (1997), The transition from brittle faulting to cataclastic flow in porous sandstones: Mechanical deformation, *J. Geophys. Res.*, *102*, 3009–3025.

N. Brantut and A. Schubnel, Laboratoire de Géologie, École Normale Supérieure, 24 rue Lhomond, F-75231 Paris, CEDEX 05, France. (nicolas.brantut@ens.fr)

J. Sulem, CERMES, UR Navier, CNRS, UMR 8205, École des Ponts ParisTech, Université Paris-Est, F-77454 Marne-la Vallée, France.